Appl Phys B (2010) 99: 449–456
DOI 10.1007/s00340-010-3978-x

Applied Physics B
Lasers and Optics

Three-dimensional data acquisition by digital correlation of projected speckle patterns

M. Dekiff · P. Berssenbrügge · B. Kemper · C. Denz · D. Dirksen

Received: 23 September 2009 / Revised version: 4 February 2010 / Published online: 17 March 2010

Abstract Reliable methods for the optical acquisition of three-dimensional (3D) coordinates like the fringe projection technique or 3D laser scanning are sensible to object movements because they require the recording of a sequence of images. In contrast, techniques using the projection of a random pattern reduce the measurement time to a single exposure time.

A method is presented which allows the 3D acquisition of a surface from a single stereo image pair by projecting a laser speckle pattern. The use of a laser enables a simple design of the projection device as well as a suppression of ambient light by narrow band-pass filtering. Corresponding image points are determined by a digital image correlation algorithm. In order to optimize the introduced method, the influence of various parameters on the number and accuracy of the determined 3D coordinates is analyzed on the basis of comparative measurements with the fringe projection technique. It is demonstrated that the introduced approach allows the acquisition of 3D data of skin surfaces.

M. Dekiff (✉) · P. Berssenbrügge · D. Dirksen
Department of Prosthetic Dentistry, University of Münster, Waldeyerstr. 30, 48149 Münster, Germany
e-mail: markus.dekiff@uni-muenster.de
Fax: +49-251-8347182

P. Berssenbrügge
e-mail: berssenbruegge@uni-muenster.de

D. Dirksen
e-mail: dirksdi@uni-muenster.de

B. Kemper
Center for Biomedical Optics and Photonics, University of Münster, Robert-Koch-Str. 45, 48129 Münster, Germany
e-mail: bkemper@uni-muenster.de

C. Denz
Institute of Applied Physics, University of Münster, Corrensstr. 2, 48149 Münster, Germany
e-mail: denz@uni-muenster.de

1 Introduction

Photogrammetry allows the acquisition of three-dimensional (3D) coordinates from (at least two) photographic images by triangulation. It represents a non-contact, non-destructive technology to measure object surfaces. A crucial step in this process is the identification of corresponding image points in the individual images. In order to automate this analysis and to increase the reliability, resolution and accuracy of the results, pattern projection techniques are widely used. Perhaps the most common approach is the fringe projection technique [1–3]. It uses a sequence of binary and/or sinusoidal fringe patterns which allows a localization of surface points in the recorded digital images with subpixel accuracy and automatic calculation of a high-resolution cloud of 3D coordinates. Due to its sequential recording process, it is quite sensible to object movements. Similar results can be obtained by laser scanning, where a single line of laser light is swept across the object, which takes even more time at high resolutions. Therefore, techniques are desirable that allow the automated acquisition of 3D coordinates from a single (stereo-) image pair. In this way, the measurement time will be reduced to the single exposure time of the cameras, thus enhancing the reliability of non-stationary measurements.

Proposed approaches include the projection of a single coded or random light pattern [4–7]. In material analysis, spray paint is widely used to create a random pattern that is fixed to the surface. Thus, not only the shape but also displacements and strains can be measured [8–11]. However, for in vivo measurements, e.g. of skin surfaces, this approach is unsuitable.

In this contribution a method is presented that utilizes a laser speckle pattern [12] instead. While in speckle metrology usually the analyzed speckle pattern is formed at the surface of the object under investigation, e.g. in digital speckle photography [13, 14], in our approach the speckle pattern is generated by a ground glass and projected onto the object's surface. As the pattern is monochromatic, the influence of ambient light can be minimized by equipping the cameras with suitable band-pass filters. Compared to the use of video projectors, this approach offers the prospect of simpler and more compact systems.

2 Theoretical background of photogrammetry and digital image correlation

A reasonable model to describe image formation with commonly used lenses is the pinhole camera model [15]. The relationship between a point $\mathbf{M} = (X, Y, Z)^{\mathrm{T}}$ in space and its projection $\mathbf{m}$ in the image plane of a camera with pixel coordinates $(u, v)^{\mathrm{T}}$ (Fig. 1) can be described in homogeneous coordinates by

$$s \cdot \begin{pmatrix} u \\ v \\ 1 \end{pmatrix} = \underbrace{\begin{bmatrix} f_u & 0 & p_u \\ 0 & f_v & p_v \\ 0 & 0 & 1 \end{bmatrix}}_{\mathbf{K}} \cdot \underbrace{\begin{bmatrix} r_{11} & r_{12} & r_{13} & t_1 \\ r_{21} & r_{22} & r_{23} & t_2 \\ r_{31} & r_{32} & r_{33} & t_3 \end{bmatrix}}_{[\mathbf{R}|\mathbf{t}]} \cdot \begin{pmatrix} X \\ Y \\ Z \\ 1 \end{pmatrix}, \tag{1}$$

where s is an arbitrary scaling factor. The parameters of the translation vector $\mathbf{t} = (t_i)$ and the rotation matrix $\mathbf{R} = [r_{ij}]$ relate the world coordinate system (XYZ) to the camera coordinate system $(X_{\mathrm{C}}Y_{\mathrm{C}}Z_{\mathrm{C}})$ and are referred to as *external* camera parameters. The camera calibration matrix $\mathbf{K}$ on the other hand includes the *internal* camera parameters. f_u and f_v represent the focal length f of the camera in terms of (horizontal and vertical) pixel dimensions, i.e. the distance between the image plane and the center of projection $\mathbf{C}$ (the camera center, which is also the origin of the camera coordinate system). $(p_u, p_v)^{\mathrm{T}}$ describes the position of the principal point $\mathbf{p}$, i.e. the intersection point of the image plane and the line through the camera center perpendicular to the image plane, in terms of pixel dimensions.

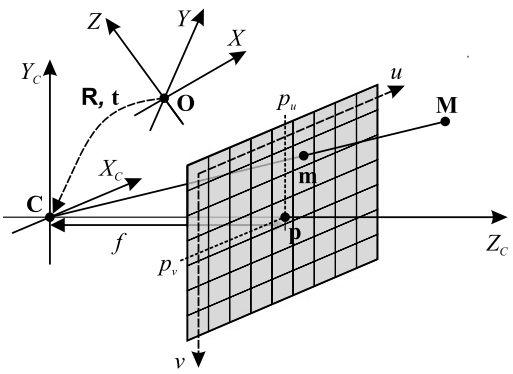

Fig. 1 Mapping of a point $\mathbf{M} = (X, Y, Z)^{\mathrm{T}}$ in space to its image $\mathbf{m} = (u, v)^{\mathrm{T}}$ in the image plane

The internal and external parameters as well as additional parameters describing lens distortions are determined in a calibration process. For this purpose, we use the approach of Zhang [16], which only requires an easy-to-manufacture plane calibration object.

In order to calculate 3D data, at least two images of the object under investigation from different points of view are required, in which an identification of corresponding image points, i.e. points that are images of the same 3D point, can be performed. In our case two cameras are used, recording a pair of stereo images. Solving (1) for object coordinates X, Y, Z in such a stereo case leads to a (overdetermined) system of four equations, which can be solved, e.g. by utilizing singular value decomposition (SVD) [17], thus obtaining a least squares solution.

While in conventional photogrammetry the identification of corresponding image points is done manually, here the digital image correlation technique (DIC) [18, 19] is applied. This method has been widely used for deformation analysis but may also be applied to determine stereo image correspondences [8–11, 20]. Its principle consists in matching subsets of different digital images by maximizing an appropriate similarity parameter. Depending on the shape of the object surface and the chosen perspectives, the corresponding image regions might differ considerably. Hence, a DIC algorithm for large deformations proposed by Lu and Cary [21] is used.

In order to determine the point (u_0', v_0') in the second image that corresponds to an image point (u_0, v_0) in the first image, a square subset around (u_0, v_0) in the first image is analyzed. Following [21], the mapping of each point (u, v) in this subset to the position of the corresponding point (u', v') in the second image is approximated by

$$u' = u + U_0 + U_u \Delta u + U_v \Delta v + \frac{1}{2} U_{uu} \Delta u^2 + \frac{1}{2} U_{vv} \Delta v^2 + U_{uv} \Delta u \Delta v, \tag{2a}$$

$$v' = v + V_0 + V_u \Delta u + V_v \Delta v + \frac{1}{2} V_{uu} \Delta u^2 + \frac{1}{2} V_{vv} \Delta v^2 + V_{uv} \Delta u \Delta v, \tag{2b}$$

with $\Delta u = u - u_0$, $\Delta v = v - v_0$. (U_0, V_0) describes the displacement of the subset center in relation to (u_0, v_0), which

leads to the sought-after point (u'_0, v'_0). U_u, U_v, V_u, V_v are the components of the first-order displacement gradient and $U_{uu}, U_{vv}, U_{uv}, V_{uu}, V_{vv}, V_{uv}$ are the components of the second-order displacement gradient. In order to compensate a possible intensity offset between the observed subset in the first image and the corresponding region in the second image, a parameter W is introduced.

Let the 13 mapping parameters $U_0, V_0, U_u, U_v, V_u, V_v, U_{uu}, \ldots, V_{uv}, W$ be the components of a vector $\mathbf{P}$ and let $f(u, v)$ and $g(u, v)$ be the discrete gray level distributions of the first and second images, respectively. Then the optimum values for the mapping parameters for a $(2m + 1) \times (2m + 1)$ pixels subset of the first image are determined by minimizing the least squares correlation coefficient [19, 21]

$$C(\mathbf{P}) = \frac{\sum_{u=-m}^{m} \sum_{v=-m}^{m} [f(u, v) - [g(u', v') - W]]^2}{\sum_{u=-m}^{m} \sum_{v=-m}^{m} [f(u, v)]^2}. \quad (3)$$

This is done numerically by calculating the roots of its gradient $\nabla C(\mathbf{P})$. For this purpose, we use an algorithm based on Powell's hybrid method [22]. In this process the necessary Hessian matrix $\nabla\nabla C(\mathbf{P})$ is approximated as proposed by Vendroux and Knauss [19] to reduce the computational effort. The calculation of $\nabla C(\mathbf{P})$ requires knowledge of gray levels at positions between pixels in the second image. Furthermore, $\nabla g(u', v')$ has to be known to calculate $\nabla C(\mathbf{P})$ and $\nabla\nabla C(\mathbf{P})$. For these purposes, bicubic spline interpolation is applied.

In order to simplify the correspondence analysis, the image pair is rectified in advance. This means that the image planes of both cameras are transformed in such a way that pairs of conjugate epipolar lines become collinear and parallel to (in our case) the horizontal image axis [23]. In the resulting rectified images, corresponding image points are located on the same horizontal line and the correspondence search can therefore be reduced to a search along an image row. Thus, for rectified images as described above, (2b) can be reduced to $v' = v$, so that only seven instead of 13 mapping parameters remain to be calculated. This leads to a reduction of computational complexity and a more stable numerical configuration.

3 Experimental setup

Figure 2 shows the experimental setup. The beam of a Nd:YAG cw laser with a wavelength of 532 nm and a maximum power of 21 mW (LCS-DTL-112A from Lasercompact, Moscow, Russia) is focussed by a lens (f = 80 mm) and passes a ground glass that generates a speckle pattern. This speckle pattern is projected onto the object under investigation and recorded by two monochrome CCD cameras with a spatial resolution of 1280 × 960 pixels and 256 gray levels (DMK 41BF02 from The Imaging Source, Bremen, Germany). Equipped with 25 mm 1:1.4 C-Mount lenses (Pentax B2514D(TH), selected aperture: 5.6) the cameras are connected to a computer (via IEEE 1394 interfaces) which is used to control the cameras and to evaluate the data.

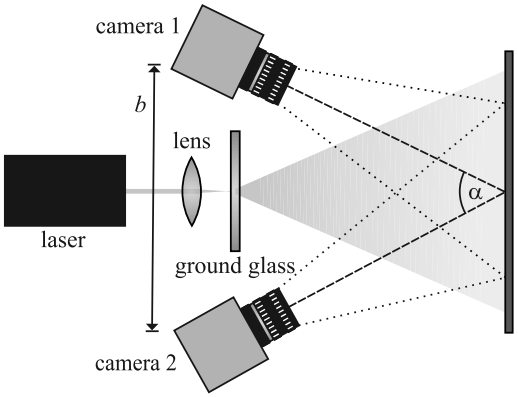

Fig. 2 Top view of the experimental setup. α is the triangulation angle, b the distance between the cameras' centers of projection

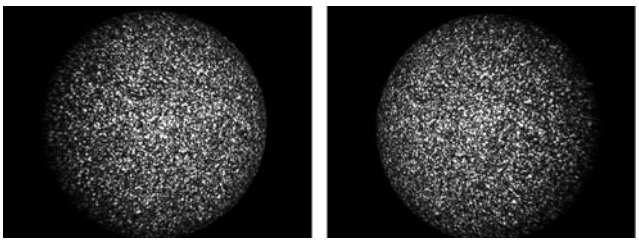

Fig. 3 Images of camera 1 (*left*) and camera 2 (*right*) recorded in the described experimental setup showing a spherical surface illuminated by a laser speckle pattern

The average size of the projected speckles is adjusted by changing the distance between lens and ground glass (in the direction of the optical axis), the image brightness by regulating the power of the laser and the exposure time of the cameras. If not stated otherwise, a power of 18 mW and an exposure time of 0.25 s are chosen. The distance between measurement system and object under investigation amounts to 100 cm, the cameras are separated by $b = 54$ cm. Thus, a triangulation angle of $\alpha \approx 30°$ results. The size of the measuring field is approximately 24×18 cm^2.

For the optimization analysis, a white painted skittles ball with a radius of 9 cm serves as test object. A typical pair of measurement images acquired by the described experimental setup is shown in Fig. 3. In order to determine the accuracy of the introduced measurement system, comparison measurements using the fringe projection technique [3] are performed employing an additional video projector (NEC LT170) placed between the cameras.

For camera calibration, a plane pattern of 48 circular marks with known coordinates is recorded in five different orientations with each camera. From these images the inter-

nal and external parameters as well as the lens distortion parameters are calculated for both cameras. The exterior orientations of the cameras referring to a common world coordinate system are calculated from an image pair of the calibration pattern that is recorded simultaneously with both cameras. Once the camera system is calibrated, an image pair of the object under investigation illuminated with a speckle pattern is taken. The calibration data are used to rectify these measurement images and to remove lens distortions. As for all further computations that require an evaluation of subpixel gray levels, bicubic spline interpolation is utilized. Afterwards, the original and the processed images are low-pass filtered in order to eliminate high-frequency noise (see Sect. 4.2). Then a grid of points with vertical and horizontal distances of 22 pixels in the first camera's (rectified and undistorted) image is defined. These points are processed row-wise, and the corresponding image points in the second camera's image are determined by correlation.

The correlation process consists of two steps. First, a rough estimate of the horizontal displacement U_0 and the first-order displacement gradient U_u is determined because these are empirically the dominating mapping parameters. For this purpose, the correlation coefficient $C(\mathbf{P})$ is calculated for a series of values for U_0 and U_u from predefined intervals while all other mapping parameters are set to zero. The parameter set that results in the smallest correlation coefficient gives a first estimate for the position of the corresponding point in the second image.

The iterative correlation algorithm is basically implemented as described in Sect. 2. The roots of the gradient of the correlation coefficient are obtained by a routine based on the MINPACK routine HYBRDJ [22]. In order to avoid numerical errors, the gray levels for calculating the gradient and the Hessian matrix of the correlation coefficient are directly determined from the original (un-rectified, but low-pass-filtered) images [20]. After the correspondence analysis is completed, outliers are removed based on the presumption that the order of points along an epipolar line in one image is the same as the order of the corresponding points on the corresponding epipolar line in the other image. Finally, the associated 3D points are computed from valid correspondences as described in Sect. 2.

For the comparison of the measurement results that are obtained with different experimental parameters (see Sect. 4), three parameters are introduced: (i) the total number of (presumably valid) found correspondences n_c, (ii) the average Euclidian deviation $\bar{\delta}$ of the 3D data determined by correlation to reference data obtained by the fringe projection technique, (iii) a parameter denoted as the correspondence index κ, which combines n_c and $\bar{\delta}$. In order to prevent outliers that were not detected automatically from dominating the average deviations, the data with deviations exceeding the 90th percentile are ignored in averaging (this value has proven to be an adequate choice). We define the parameter κ as

$$\kappa = \left(\frac{n_c}{n_r}\right)^2 \cdot \bar{\delta}^{-1}, \tag{4}$$

where n_r denotes the number of reference points. Using a sampling raster with horizontal and vertical spacings of 22 pixels, the fringe projection technique allows the calculation of about 1200 3D points of the sphere's surface in the previously described experimental setup. The ratio of found correspondences to reference points is squared to increase its influence on the correspondence index. A larger value of κ is interpreted as an indicator for a better measurement in terms of accuracy and density of obtained 3D points.

The average speckle size is determined based on the two-dimensional autocorrelation function of a selected region of interest (after filtering). The row in which the autocorrelation function reaches its maximum is approximated by a fitting function that combines a Gaussian function with a second-order polynomial. We define the full width at half maximum of this Gaussian function as the average speckle size.

4 Experimental results and discussion

4.1 Subset and speckle size

First, the influence of the average speckle size and the size of the subsets in the correlation process is investigated. For this purpose, a series of measurements with average speckle sizes ranging from 3.0 to 19.5 pixels is evaluated using subsets with widths between nine and 63 pixels.

The images are filtered with an ideal low-pass filter ($\varepsilon = 1.0$, see Sect. 4.2).

Figure 4 shows (a) the average deviation $\bar{\delta}$ of the calculated 3D points from the reference data, (b) the number of found correspondences n_c and (c) the correspondence index κ vs. the width of the square subsets for different average speckle sizes. The smallest average deviations can be achieved by using small speckles together with a subset width in the range from 21 to 33 pixels. The largest numbers of correspondences are found for medium and large speckles combined with medium or large subsets (Fig. 4b). As indicated by the correspondence index κ (Fig. 4c), the best results are obtained by using speckles with an average diameter of 7.2 pixels in combination with a 33×33 pixels subset ($\bar{\delta} = 0.103$ mm, $n_c = 889$).

The results which are depicted in Fig. 4 show that the sizes of the speckles and of the subsets considerably influence the number of found correspondences and the accuracy. With increasing subset size as well as with decreasing speckle size, the subsets contain more information in terms

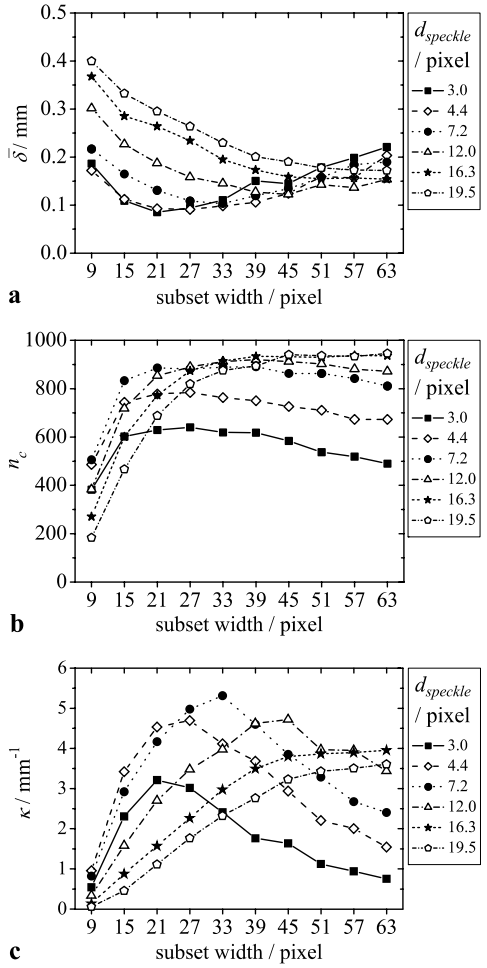

Fig. 4 Average deviation $\bar{\delta}$ (**a**), number of found correspondences n_c (**b**) and correspondence index κ (**c**) as functions of the subset width for different average speckle sizes d_{speckle}

of gray level variation. This results in a higher accuracy and a larger number of successfully determined correspondences as long as the speckles do not become too small or the subsets too large. The projected speckles should be larger than occurring subjective speckles and other forms of noise, in our case on average at least 4.4 pixels. This allows the noise to be removed efficiently by low-pass filtering without removing the projected speckles (the signal/information), too. The subsets should be small enough to enable the description of the real transformation by the mapping approach used. This requirement implies that the optimal subset size depends on the shape of the object (the flatter the surface, the larger the subsets can be chosen). Furthermore, if the speckles are too small in relation to the subsets, it will be more likely that the correlation algorithm will fail.

4.2 Image filtering

Due to the coherence of the laser light, subjective speckles occur in the measurement images in addition to the projected speckle pattern. These subjective speckle patterns in both images are different and thus are expected to affect the correlation process. Hence, the application of several digital image filters is investigated. A Gaussian filter, an average filter and a median filter as well as an ideal low-pass and a second-order Butterworth low-pass filter are applied. The amount of the smoothing effect for the first three filter types is adjusted by the width of the filter window/kernel a_{filter}. The effect of the ideal low-pass filter and the Butterworth low-pass filter is specified by their cut-off frequency υ_0 that we define as

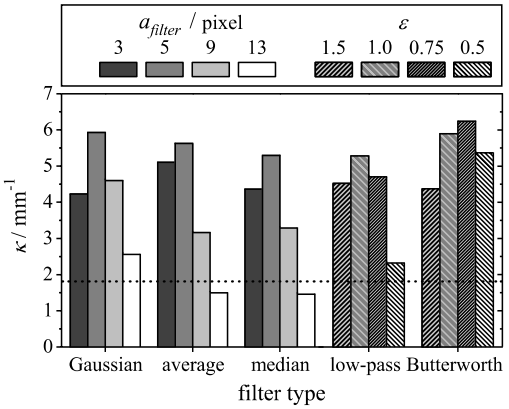

Fig. 5 Correspondence index κ for different types of digital filters ('low-pass' = ideal low-pass filter; 'Butterworth' = Butterworth low-pass filter). The *dotted line* shows the resulting value of κ without filtering

$$\upsilon_0 := \varepsilon \frac{|x_W - x'_W|}{2}, \tag{5}$$

where ε is an arbitrary but non-negative value and x_W and x'_W are the abscissae of the turning points of a Gaussian fitting function to the row-wise summed up absolute values of the Fourier transform of the image. According to their definitions, larger values for a_{filter} as well as smaller values for ε mean stronger smoothing. In order to determine appropriate values for ε and a_{filter}, a measurement with an average speckle diameter of 7.2 pixels (for an ideal low-pass filter, $\varepsilon = 1.0$) is evaluated with 33×33 pixels subsets and different filter settings.

Figure 5 shows the correspondence index κ for the investigated filter configurations. The best results are obtained with the Butterworth low-pass filter with $\varepsilon = 0.75$. Compared to the results obtained without filtering ($\bar{\delta} = 0.192$ mm, $n_c = 704$), the average deviation is reduced by 50% and the number of found correspondences is increased by 33% ($\bar{\delta} = 0.097$ mm, $n_c = 934$).

These results clearly show that the high-frequency noise originating from various sources like subjective speckles, quantization error, sensor noise, etc., strongly complicates the correlation process. This noise differs between images;

thus, it reduces the similarity between corresponding image areas and therefore makes appropriate filtering a crucial preprocessing step. However, overdoing smoothing may worsen the result as too much information (gray level variation) is lost. Hence, the filter parameters have to be chosen carefully considering the size of the structures to eliminate or to preserve.

4.3 Triangulation angle

The perspective differences between both cameras can be reduced by decreasing their distance b (Fig. 2). In this way, a more accurate correspondence analysis may be expected but, on the other hand, reducing the triangulation angle α results in an increased triangulation error [24]. In order to evaluate the influence of the triangulation angle α, four measurements with different distances b are carried out. The images are filtered by a Butterworth low-pass filter ($\varepsilon = 0.75$) as this filter turned out to be the best approach in the previous analysis. The average speckle diameter is 8.5 pixels (this corresponds to a speckle diameter of 7.2 pixels after filtering with the ideal low-pass filter and $\varepsilon = 1.00$), and subsets of 33×33 pixels are used. For each triangulation angle, a comparative measurement with the fringe projection method is performed.

The number of found correspondences n_c and the average deviation both for all found correspondences $\bar{\delta}$ and for those ones localized in the center area of the field of view $\bar{\delta}'$ are depicted for four different triangulation angles in Fig. 6. The results show that n_c decreases almost linearly with an increasing triangulation angle α. The average deviation in the center of the field of view decreases monotonically. Likewise, the overall average deviation decreases, at least for small to medium angles. A triangulation angle of $\approx 22°$ turns out to be an appropriate compromise between accuracy and amount of measured 3D points.

These results qualitatively meet the expectations, i.e. a smaller angle reduces the perspective differences and therefore simplifies the correspondence analysis. Thus, more correspondences are found, which additionally are presumably more accurate than those obtained with larger triangulation angles. Of course, the increase in the number of found correspondences also traces back to the fact that the overlap of the surface areas which are imaged by both cameras is larger for smaller triangulation angles. Nevertheless, due to the increasing triangulation error (for decreasing triangulation angles) the deviations of the calculated 3D coordinates are larger. For our measurements of a sphere, a triangulation angle of around 22° turns out to be an appropriate compromise but, depending on the depth structure of the object, a smaller or larger angle may be preferred.

4.4 Brightness of the imaged speckle pattern

To investigate the influence of the image brightness on the correlation algorithm, a series of measurements with different laser intensities is carried out. The images are filtered with a Butterworth low-pass filter ($\varepsilon = 0.75$), the subset width amounts to 33 pixels and the average speckle size to 8.5 pixels. An exposure time of 2 s is chosen. The brightness of the imaged speckle pattern is defined as the average gray level $\bar{g}$ in a subset of 600×600 pixels around the center of the image of camera 1.

In Fig. 7 the average deviation $\bar{\delta}$ and the number of found correspondences n_c are depicted as functions of the average gray level $\bar{g}$ of the imaged speckle pattern. The curves show that n_c increases with increasing brightness while $\bar{\delta}$ decreases until an average gray level of approximately 100, then rises again and finally starts to fluctuate. The correspondence index κ (not shown) indicates that the best overall results are obtained for $\bar{g} \approx 170$ and $\bar{g} \approx 180$.

In order to evaluate whether it is possible to improve the results of measurements with dark speckle patterns by a subsequent scaling of the gray levels, the images of a measurement with $\bar{g} \approx 12$ are scaled to an average gray level of 175 by multiplying the gray levels with a factor of 23 before filtering (values higher than 255 are reduced to 255). Evaluating these modified images results in similar values for n_c and

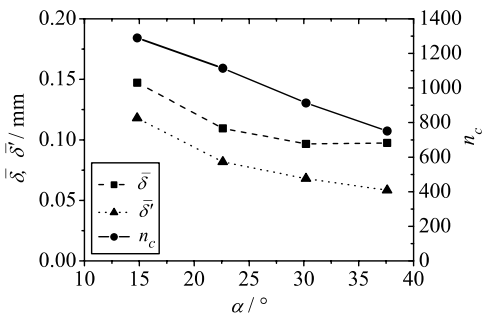

Fig. 6 Number of found correspondences n_c, average deviation for all found correspondences $\bar{\delta}$ and for those located in the center of the field of view $\bar{\delta}'$ as functions of the triangulation angle α

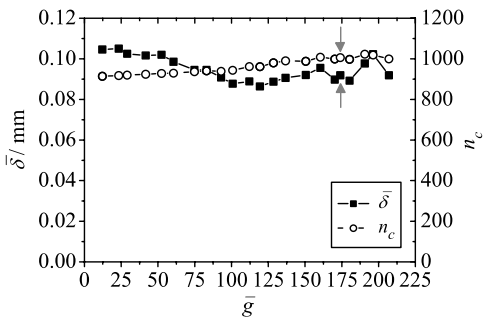

Fig. 7 Average deviation $\bar{\delta}$ and number of found correspondences n_c as functions of the average gray level $\bar{g}$ of the imaged speckle pattern. The data points marked by *arrows* are obtained by rescaling the gray levels

$\bar{\delta}$ as obtained with the original measurement with $\bar{g} \approx 170$ (Fig. 7).

With increasing intensities dark speckles become more visible, but at the same time bright speckles are overexposed and gray level variations are clipped. However, the stronger weighting of darker speckles seems to compensate the loss of information from clipping. A reason could be that the uniformity of the distribution of speckles in the subsets increases, thus allowing a more precise and robust correspondence analysis. As the results show, raising the image brightness after the measurement by multiplying the gray levels and cutting off values over 255 leads to the same positive effects as increasing the laser light intensity. The scaling also amplifies the noise and can reduce the number of occurring gray scales, but these drawbacks are mostly compensated by low-pass filtering afterwards.

4.5 Comparison with the fringe projection technique

In order to compare the accuracy of the presented speckle correlation method with that of the fringe projection technique, a sphere function is fitted to both the 3D data resulting from the speckle correlation measurement with $\bar{g} \approx 180$ in Sect. 4.4 and the reference data. It is assumed that the investigated skittles ball (radius: 90.0 ± 0.5 mm) represents an ideal sphere. The fit results for the speckle correlation method in a radius of 89.96 mm. The corresponding average deviation of the measured data is 0.058 mm.

For the reference data obtained by the fringe projection technique, a radius of 89.93 mm and an average deviation of 0.019 mm are determined. These results indicate that fringe projection yields an approximately three times higher accuracy compared to speckle correlation. Furthermore, it supports the assumption that 3D data acquired by fringe projection can be used as reference data.

The lateral resolution that can be obtained by the fringe projection method corresponds to one pixel/image height. In the case of the speckle correlation method, this figure is limited by the chosen subset size [25]. In the presented case, a minimum of approximately 20×20 pixels is required to obtain both a sufficient accuracy and a reasonable number of 3D data points.

4.6 Acquisition of the shape of a human hand

In order to demonstrate the application of the technique for measuring skin surfaces, the shape of a hand is acquired. For this purpose, the palm is aligned orthogonally to the optical axis of the camera system. Based on the previously described results, a triangulation angle of 23° is used. The average speckle size is chosen to be eight pixels, the subset width amounts to 33 pixels. With an exposure time of 1 s and a laser power of 20 mW (the intensity on the skin is less than 0.4 W/m^2), an average gray level of 30 results, which is scaled up to 95 for the correspondence search. The images are filtered by a Butterworth low-pass filter ($\varepsilon = 0.75$). Using a sampling raster with horizontal and vertical spacings of 11 pixels, 3900 3D points are obtained. Figure 8 shows the result. It demonstrates that the method is able to acquire the surface of dermal surfaces in vivo.

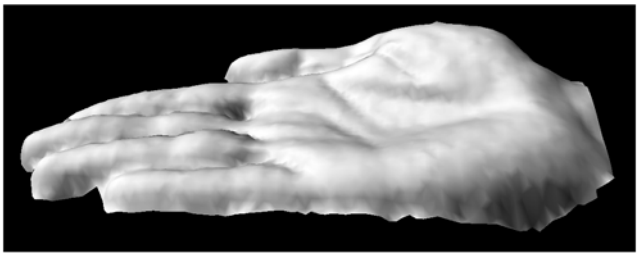

Fig. 8 Result of a measurement of a hand

5 Conclusion

A technique has been presented that allows the acquisition of the 3D shape of a surface from a single stereo image pair through digital image correlation, employing a projected laser speckle pattern. It is demonstrated that noise arising from subjective speckles can be suppressed by appropriate low-pass filtering. Parameters like the triangulation angle, the size of the subsets in the correlation process and the average speckle size, which influence the resulting accuracy as well as the number of calculated 3D points, have been optimized. On the other hand, the average brightness of the speckles showed only minor influence.

As demonstrated by a sample measurement, the presented approach is capable of obtaining 3D data of skin surfaces. However, due to the particular optical properties of skin, further investigations are necessary to optimize the presented technique for this application. Compared to white light techniques like fringe or random pattern projection methods, the achievable accuracy is significantly lower due to laser speckle noise, although further improvements of accuracy and robustness might be achieved, e.g. by an adaptive subset size [26] and the use of rotating ground glasses in front of the cameras to reduce subjective speckles in the images. An advantage of the speckle correlation approach is the achievable measurement time, which only depends on the illumination intensity. Using a pulsed laser, the measurement time could be easily reduced to less than a microsecond. Post processing in its current (non-optimized) implementation still takes several minutes (fringe projection technique: <2 s), but the performance will benefit automatically from future faster hardware.

However, the key advantages of the presented method are its robustness against ambient light when using appropriate

narrow band-pass filters and the simple optical setup, which is particularly suited for combination with other laser based measurement techniques like electronic speckle pattern interferometry (ESPI).

References

1. F. Chen, G.M. Brown, M. Song, Opt. Eng. **39**, 10 (2000)
2. C. Reich, R. Ritter, J. Thesing, Opt. Eng. **39**, 224 (2000)
3. G. Bischoff, Z. Böröcz, C. Proll, J. Kleinheinz, G. von Bally, D. Dirksen, Biomed. Tech. **52**, 284 (2007)
4. J. Salvi, J. Pagès, J. Batlle, Pattern Recogn. **37**, 827 (2004)
5. P. Azad, T. Gockel, R. Dillmann, in *Proc. ITCC04*, vol. 2, p. 367 (2004)
6. B. Pan, H. Xie, J. Gao, A. Asundi, Appl. Opt. **47**, 5527 (2008)
7. N. D'Apuzzo, Proc. SPIE **4661**, 191 (2002)
8. Z.L. Kahn-Jetter, T.C. Chu, Exp. Mech. **30**, 10 (1990)
9. P.F. Luo, Y.J. Chao, M.A. Sutton, W.H. Peters III, Exp. Mech. **33**, 123 (1993)
10. J. Helm, S. McNeill, M. Sutton, Opt. Eng. **35**, 1911 (1996)
11. L. Robert, F. Nazaret, T. Cutard, J.-J. Orteu, Exp. Mech. **47**, 761 (2007)
12. J.W. Goodman, in *Laser Speckle and Related Phenomena*, ed. by J.C. Dainty (Springer, Berlin, 1975), p. 9
13. M. Sjödahl, H.O. Saldner, Appl. Opt. **36**, 3645 (1997)
14. T. Fricke-Begemann, Appl. Opt. **42**, 6783 (2003)
15. R. Hartley, A. Zisserman, *Multiple View Geometry in Computer Vision* (Cambridge University Press, Cambridge, 2003)
16. Z. Zhang, Microsoft Research Tech. Rep. MSR-TR-98-71 (1998)
17. W.H. Press, S.A. Teukolsky, W.T. Vetterling, B.P. Flannery, *Numerical Recipes in C*, 2nd edn. (Cambridge University Press, Cambridge, 1992)
18. H.A. Bruck, S.R. McNeil, M.A. Sutton, W.H. Peters, Exp. Mech. **29**, 261 (1989)
19. G. Vendroux, W.G. Knauss, Exp. Mech. **38**, 86 (1998)
20. D. Garcia, Mesure de formes et de champs de déplacements tridimensionnels par stéréo-corrélation d'images. Ph.D. thesis, Institut National Polytechnique de Toulouse (2001)
21. H. Lu, P.D. Cary, Exp. Mech. **40**, 393 (2000)
22. J.J. Moré, B.S. Garbow, K.E. Hillstrom, User Guide for MINPACK-1. Argonne National Laboratory Rep. ANL-80-74 (1980)
23. A. Fusiello, E. Trucco, A. Verri, Vis. Appl. **12**, 16 (2000)
24. K. Kraus, *Photogrammetry*. Fundamentals and Standard Processes, vol. 1 (Dümmlers, Bonn, 1993)
25. M. Bornert, F. Brémand, P. Doumalin, J.-C. Dupré, M. Fazzini, M. Grédiac, F. Hild, S. Mistou, J. Molimard, J.-J. Orteu, L. Robert, Y. Surrel, P. Vacher, B. Wattrisse, Exp. Mech. **49**, 353 (2009)
26. T. Kanade, M. Okutomi, IEEE TPAMI **16**, 920 (1994)